

---

# A MULTIMODAL APPROACH COMBINING STRUCTURAL AND CROSS-DOMAIN TEXTUAL GUIDANCE FOR WEAKLY SUPERVISED OCT SEGMENTATION

---

A PREPRINT

**Jiaqi Yang\***  
CUNY Graduate Center

**Nitish Mehta**  
New York University Department of Ophthalmology  
NYU Langone Health

**Xiaoling Hu**  
Massachusetts General Hospital  
and Harvard Medical School

**Chao Chen**  
Stony Brook University

**Chia-Ling Tsai**  
CUNY Queens College

November 20, 2024

## ABSTRACT

Accurate segmentation of Optical Coherence Tomography (OCT) images is crucial for diagnosing and monitoring retinal diseases. However, the labor-intensive nature of pixel-level annotation limits the scalability of supervised learning with large datasets. Weakly Supervised Semantic Segmentation (WSSS) provides a promising alternative by leveraging image-level labels. In this study, we propose a novel WSSS approach that integrates structural guidance with text-driven strategies to generate high-quality pseudo labels, significantly improving segmentation performance. In terms of visual information, our method employs two processing modules that exchange raw image features and structural features from OCT images, guiding the model to identify where lesions are likely to occur. In terms of textual information, we utilize large-scale pretrained models from cross-domain sources to implement label-informed textual guidance and synthetic descriptive integration with two textual processing modules that combine local semantic features with consistent synthetic descriptions. By fusing these visual and textual components within a multimodal framework, our approach enhances lesion localization accuracy. Experimental results on three OCT datasets demonstrate that our method achieves state-of-the-art performance, highlighting its potential to improve diagnostic accuracy and efficiency in medical imaging.

**Keywords** Weakly supervised semantic segmentation · Vision-Language models · Retinal OCT lesion segmentation · Multimodal learning · Structural guidance

## 1 Introduction

Semantic segmentation, a key computer vision task, categorizes each pixel in an image and has applications across diverse fields, including autonomous driving, geospatial analysis, and medical imaging. In retinal lesion segmentation, automating the identification of lesions and retinal conditions can significantly improve clinical diagnosis and management. Optical Coherence Tomography (OCT) is an essential imaging modality, providing high-resolution, cross-sectional retina images for enhanced detection and monitoring of retinal diseases. Recognizing and segmenting these lesions in clinical practice facilitates treatment planning and offers a nuanced understanding of disease activity [Schmidt-Erfurth et al., 2021]. By highlighting lesions as diagnostic and prognostic biomarkers, these technologies lead to better patient outcomes.

---

\*Email: jyang2@gradcenter.cuny.edu

In most cases, fully-supervised learning is the standard approach, where models are trained with precise pixel-level annotations to achieve accurate segmentation. However, obtaining precise pixel-level annotations is always labor-intensive and costly in medical imaging, where domain expertise is required. In addition to the sheer amount of data for annotation, pixel-level labeling of lesions with ill-defined boundaries poses additional challenges for segmentation due to high inter-expert variability, particularly for OCT images. The difficulty in obtaining consistent and reliable annotations for big data motivates the exploration of alternative segmentation methods that demand weak supervision at the image level as experts have higher agreement in lesion presence, compared to lesion extent.

Weakly supervised semantic segmentation (WSSS) has emerged as a promising research direction. WSSS leverages weak forms of supervision, such as image-level labels [Pinheiro and Collobert, 2015, Ahn and Kwak, 2018, Kolesnikov and Lampert, 2016, Kwak et al., 2017, Niu et al., 2023], scribbles [Lin et al., 2016, Vernaza and Chandraker, 2017, Luo et al., 2022, Valvano et al., 2021], bounding boxes [Ma et al., 2022, Oh et al., 2021, Dai et al., 2015], or global constraints [Kervadec et al., 2019], to generate pixel-level predictions. Image-level WSSS has gained significant attention in medical imaging for its ability to reduce the need for detailed annotations, offering a cost-effective alternative. In this study, we aim to develop a WSSS method that utilizes only image-level supervision to segment lesions in multi-label OCT images.

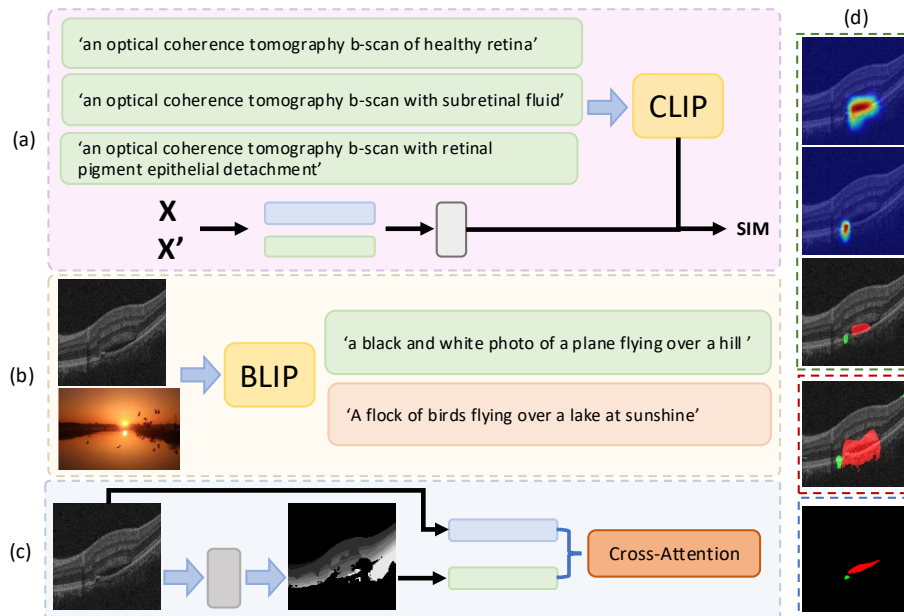


Figure 1: Visual examples of our proposed multimodal framework’s submodules. (a) Example of the proposed label-informed strategy, where  $X$  and  $X'$  represent the OCT image and structural input, respectively. (b) Synthetic text generation by BLIP, with a natural image shown for comparison; the pretrained BLIP recognizes the shape and object relationship, identifying a ‘plane’ over ‘a hill.’ (c) Example of the structural input with the cross-attention mechanism. (d) Illustration of CAMs and pseudo labels generated by our proposed method (green box), compared with pseudo labels from ResNet-50 (red box), and the ground truth (blue box) for reference. Best viewed in color.

A common strategy in WSSS involves generating class activation maps (CAMs) [Zhou et al., 2016] from a classification network to create pixel-level pseudo labels. These pseudo labels are then used to fully supervise a separate segmentation model. However, the deficiency in this approach comes from the capability of the classification model being activated by partial objects, leading to the gap between the CAM and the actual object for segmentation. Motivated by the challenges of weak supervision, we propose a WSSS model incorporating textual and structural information beyond image-level labels to enrich the model training process and achieve more precise segmentation results, as shown in Fig. 1.

We leverage foundation models for their ability to capture rich semantic information from diverse data, enhancing our model by providing stronger context-aware insights and reducing reliance on extensive labeled datasets. Recent studies [Lin et al., 2023, Deng et al., 2024] have demonstrated the potential of integrating textual information into WSSS using vision-language models like Contrastive Language-Image Pre-training (CLIP), which effectively links textual descriptions with corresponding image components. However, most of these models are pretrained on natural image-text pairs. Although some MedCLIP works, such as Wang et al. [2022], have fine-tuned CLIP with medical

data, the OCT modality remains underexplored, and relevant image-text pairs are even more scarce. Therefore, directly applying a pretrained model to generate effective textual features for OCT images is not feasible. To effectively generate and utilize texts that align with OCT images with a pretrained foundation model, we explore two text-driven strategies: label-informed textual guidance and synthetic descriptive guidance.

The label-informed strategy leverages CLIP’s semantic labels to focus on local features, using text descriptions to identify specific lesions and their characteristics. Despite CLIP being trained on data that may not directly overlap with OCT images, it has developed a broad understanding of semantic concepts. This allows it to relate to lesions like ‘subretinal fluid’, inferring their spatial (e.g., ‘sub-’) and morphological (e.g., ‘fluid’) characteristics even in unfamiliar medical contexts. More sample texts are shown in Fig. 1 (a). By aligning CLIP’s text embeddings with the visual features of OCT images, we guide the model’s attention to relevant regions, refining the representations of corresponding lesions and improving the model’s ability to localize them.

For synthetic descriptive guidance, we propose leveraging pretrained captioning models from other datasets (e.g., natural images) to generate text descriptions for each OCT image. Unlike the label-informed strategy, this method takes a more global perspective, describing the overall appearance of the image and the relationships between objects. As illustrated by the example in the green in Fig. 1 (b), this is akin to a three-year-old describing an unfamiliar scene using familiar objects (e.g., cats and dogs). While the descriptions may lack medical precision, their consistency across similar lesions offers a supplementary signal that strengthens the weak supervision process. By integrating these synthetic texts with image-level supervision, we enhance the model’s ability to identify subtle semantic features and corresponding regions.

In addition to textual information, structural details within OCT images provide reliable guidance for precise lesion localization, drawing inspiration from how doctors assess the positional relationship between objects and retinal layers. Lesions often align with specific layers, making their positional patterns crucial for distinguishing true lesions from shadows or artifacts and for identifying different lesion types. To complement our text-driven strategies, we incorporate structural features, including weak anomalous signals that typically appear in specific positions within certain retinal layers, into the WSSS framework as shown in Fig. 1 (c). To effectively use this structural information, we introduce cross-attention modules that enable the sharing of structural features across the network while integrating the semantic context from textual insights, thereby improving the model’s accuracy in weakly supervised segmentation. Fig. 1 (d) illustrates an example where our proposed method demonstrates better performance (green box).

In summary, our main contributions are as follows:

- We introduce a novel method for multi-label WSSS of OCT images, incorporating structural features and text-driven strategies for enhanced spatial and contextual supervision.
- We incorporate structural information to direct the model’s learning towards the specific retinal layer positions associated with lesion occurrence, thereby enhancing the precision of lesion segmentation.
- To further enrich the learnable weak features, we design two complementary text-driven strategies that leverage large foundation models. The first strategy, Label-Informed Textual Guidance, employs the CLIP model to incorporate semantic labels for robust lesion representations. The second strategy, Synthetic Descriptive Integration, adapts pretrained captioning models from natural image datasets to generate consistent text descriptions that offer additional guidance.
- Following the literature, we conduct comprehensive experiments on three OCT datasets, demonstrating that our approach outperforms current state-of-the-art methods for WSSS using only image-level labels.

## 2 Related Works

### 2.1 Weakly Supervised Semantic Segmentation

The WSSS has gained significant attention due to the scarcity of expert-annotated pixel-level labels, especially in domains such as medical imaging. Most of the methods exploit CAMs to segment class objects [Zhou et al., 2016, Selvaraju et al., 2017, Wang et al., 2020a, Ramaswamy et al., 2020, Kim et al., 2021, Wang et al., 2020b, Ru et al., 2022, Chen et al., 2022a, Shi et al., 2021]. WSSS typically follows a three-stage learning process. First, a classification model is supervised using image-level labels to generate initial CAMs, which highlight the discriminative regions that influence the classification decision. C2AM [Xie et al., 2022a] proposes to apply contrastive learning for foreground and background discrimination to reduce over-activation. Next, these initial CAMs are refined using various techniques, such as dense CRF, affinity-based methods, or saliency maps [Lee et al., 2021], to enhance the quality of the pseudo labels. For instance, methods like [Wu et al., 2021] embed attention mechanisms to capture class-specific affinities, while approaches such as [Choe et al., 2020] and [Jo and Yu, 2021] expand object regions by

dropping out the most discriminative parts or removing patches from the images. Finally, the refined pseudo labels serve as ground-truth masks to train a dedicated segmentation network, often using models from the DeepLab [Chen et al., 2017a,b] series, which is then employed for inference, closely mimicking a fully supervised setup.

However, the direct application of these methods to medical images presents significant challenges due to the finer and more complex anatomical structures inherent in medical images. Unlike natural images, where objects are typically larger and more distinct, medical images often feature small, detailed regions, such as blood vessel exudates, with poorly defined boundaries between the foreground objects and the background.

**WSSS for Medical Image.** In the medical imaging domain, several CAM-based WSSS methods have been developed to refine initial CAMs and improve segmentation across various modalities [Roth et al., 2021, Wang et al., 2021, Patel and Dolz, 2022]. However, compared to the computer vision field, research on medical image segmentation using only image-level labels [Ouyang et al., 2019, Viniavskyi et al., 2020, Belharbi et al., 2021] remains limited and often relies on domain-specific knowledge. Models from one imaging modality struggle to transfer to another due to differences in image characteristics and anatomical structures. For instance, OEEM [Li et al., 2022a] enhances gland segmentation in histology images by using patch-level labels to refine the initial CAM seed, a method less applicable to OCT images with fewer target regions. Similarly, Patel et al. [Patel and Dolz, 2022] introduce a cross-modality invariant constraint that requires the availability of multiple modalities within the domain. Additionally, most existing methods in the medical image domain, particularly in OCT segmentation, focus on single biomarkers rather than multi-label tasks [Zhang et al., 2022, Liu et al., 2023, Xing et al., 2021, Wang et al., 2020c], addressing only one lesion class per image. Even though some works [Chen et al., 2022b, Yang et al., 2024] propose advanced strategies for multi-label tasks in medical imaging, they still limit their exploration to the image modality alone.

Beyond the common challenges mentioned above, medical WSSS rarely addresses the inherent limitations of image-level supervision, which carries limited information. These approaches often overlook the potential of integrating richer information beyond the visual context. In contrast, our approach leverages additional sources of information, such as structural details and multimodal data, including text. This integration enables the model to more accurately localize lesions by utilizing enriched global contextual cues.

## 2.2 Vision-Language Models

Recent advancements in pretrained large-scale vision-language models have significantly enhanced the integration of visual and textual modalities, leading to improved performance in downstream tasks. One notable model is Contrastive Language-Image Pre-training (CLIP) [Radford et al., 2021], which consists of an image encoder and a text encoder. CLIP is pretrained on a vast dataset of 400 million image-text pairs, automatically collected from the Internet without manual annotation. This extensive pretraining enables CLIP to effectively map a wide range of visual concepts to their corresponding text labels, demonstrating significant success and potential, particularly in zero-shot settings. To leverage the advantages of CLIP, subsequent works have developed MedCLIP<sup>2</sup>, a model pretrained on the ROCO medical dataset [Pelka et al., 2018] using the CLIP framework. Similarly, another version of MedCLIP [Wang et al., 2022] has been pretrained on four x-ray datasets, maintaining the core design of CLIP to enhance its performance in the medical domain. In parallel with these developments, other vision-language models like BLIP [Li et al., 2022b] have emerged, focusing on tasks such as image captioning. BLIP demonstrates strong capabilities in generating natural language descriptions of visual content. It accomplishes this by utilizing a text decoder that interprets the visual input as a question and the text generation task as its corresponding answer.

**CLIP in WSSS.** In the context of WSSS, CLIMS [Xie et al., 2022b] is the first to incorporate CLIP, utilizing the similarity scores generated by the frozen CLIP model as supervision to improve the initial CAMs gradually. Similarly, CLIP-ES [Lin et al., 2023] proposes enhancements across all three stages of the WSSS process with a special design for CLIP usage. Both CLIMS and CLIP-ES rely on the zero-shot capabilities of a frozen CLIP model, which is crucial for generating reliable textual features or similarity scores that can effectively guide segmentation in natural images. Since these methods depend on the pretrained CLIP model’s outputs, they are not directly adaptable to the OCT image domain, where the visual characteristics differ significantly. Unlike these works in natural images, we leverage CLIP’s strong generalization capabilities to adapt it for the retinal OCT domain, aligning image-text similarity through CLIP-generated textual features without relying solely on its zero-shot performance.

In the context of applying CLIP to WSSS in medical imaging, TPRO [Zhang et al., 2023] introduces a text-prompting-based WSSS method specifically designed for histopathological images, utilizing MedCLIP embeddings for label texts and ClinicalBert embeddings for knowledge texts. While TPRO adapts CLIP to medical images using domain-specific embeddings, it applies the same knowledge texts across the dataset, which may miss the nuanced variations between

<sup>2</sup><https://github.com/Kaushalya/medclip>



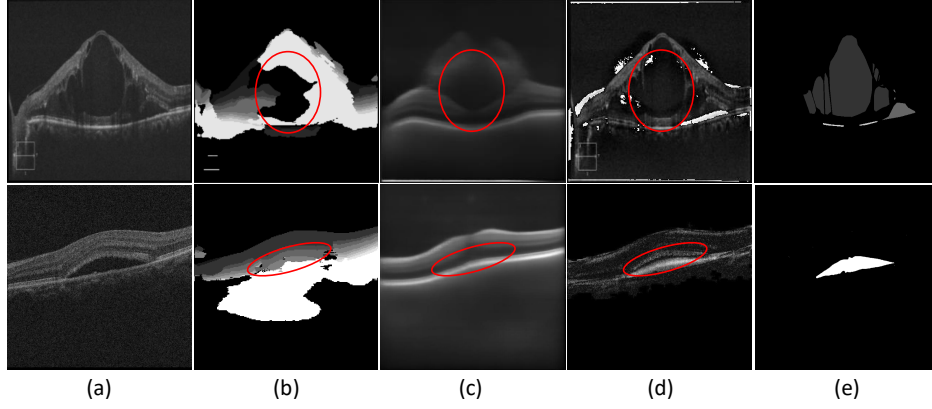


Figure 3: Visualization of pretrained models’ outputs and their relationship to lesion localization. (a) Original OCT image. (b) Pretrained model output showing layer segmentation. (c) Pretrained model output showing the GAN-generated healthy counterpart. (d) Anomalous representation. (e) Ground truth annotation. Red circles highlight the relationship between lesions and retinal layers, demonstrating how the noisy information contributes to lesion localization.

denoted as  $\mathcal{L} = (L_i, y_i)_{i=1}^N$  and  $\mathcal{A} = (A_i, y_i)_{i=1}^N$  respectively. Although the pretrained models introduce noise and artifacts, they still provide valuable guidance by capturing both the positional relationships between lesions and retinal layers, as well as identifying anomalous regions. For example, as shown in Fig. 3, while the models’ direct outputs are imperfect, they still align lesions with specific retinal layers and highlight potential abnormalities. This combined information offers critical insights for accurately locating lesions.

Similar to the primary image encoder, we employ the MiT encoder as the backbone. Consequently, we add the layer and anomaly images to ensure proper feature extraction. Thus, the input of the structural encoder is designed as:

$$X'_i = \frac{(L_i + A_i) - (L_i + A_i)_{\min}}{(L_i + A_i)_{\max} - (L_i + A_i)_{\min}} \quad (1)$$

$$\mathcal{D}' = \{(X'_i, y_i)\}_{i=1}^N, \text{ where } X'_i \in \mathbb{R}^{C \times H \times W} \quad (2)$$

where  $X'_i$  denotes the input to the structural encoder and  $\mathcal{D}'$  represents the dataset. The final output of the structural feature encoder is a set of feature maps, denoted as  $F_s^T \in \mathbb{R}^{H_s \times W_s \times C_s}$ . These feature maps are then integrated with those from the primary image encoder to provide richer structural information. Further details are provided in the next section.

**Cross-Attention Feature Exchange.** We introduce a cross-attention module to facilitate the exchange of information between the primary and structural branches. This module enables the interaction of features from both visual branches before progressing to the next encoding stage.

The structure of this module is based on the core components of the transformer block, incorporating layer normalization, multi-head attention, multi-layer perceptron (MLP), and skip connections. We utilize features from both branches to create the *Affinity* matrix, which then enhances the representation in the target branch. Taking the primary branch as an example:

$$\begin{aligned} Q &= \mathbf{W}_s^q F_s^T, K = \mathbf{W}_s^k F_s^P, V = \mathbf{W}_s^v F_s^P \\ \text{Affinity}_s^P &= \text{softmax}(QK^T / \sqrt{C_s/h}) \\ Z_s^P &= \text{Affinity}_s^P V, s \in [2, 3] \end{aligned} \quad (3)$$

where  $\mathbf{W}_s^q, \mathbf{W}_s^k, \mathbf{W}_s^v$  are learnable parameters at encoder stage  $s$ ,  $h$  is the number of heads, and  $Z_s^P \in \mathbb{R}^{H_s \times W_s \times C_s}$  represents the features after the interaction between  $F_s^T$  and  $F_s^P$  at stage  $s$ . This process is illustrated in Fig. 4.

Similarly, for the structural branch at stage  $s$ , we obtain the cross-attention enhanced feature  $Z_s^T$ . In this design, we ensure comprehensive feature exchange between both branches, effectively enhancing the primary branch with structural features that carry positional and weak anomaly signals. This enriched contextual information improves the guidance for subsequent feature processing stages during training.

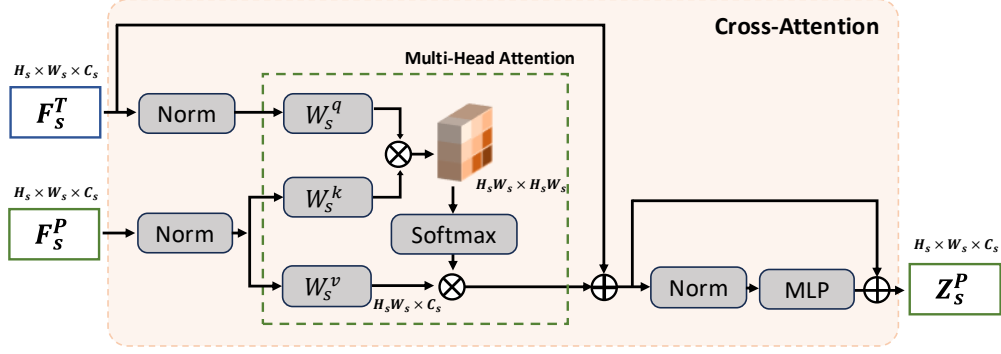


Figure 4: Structure of the Cross-Attention for the primary features, where  $H_s$ ,  $W_s$ , and  $C_s$  denote the height, width, and number of channels of feature maps at stage  $s$ , respectively.  $F_s^T$  and  $F_s^P$  represent feature maps from the structural and primary encoders, respectively.

### 3.2 Textual Processing Modules

In this section, we introduce the textual modules that leverage large foundation models for medical imaging, transforming ‘imperfections’ into valuable signals for the WSSS task. The module consists of a synthetic description module and a label-informed textual module.

**Synthetic Descriptive Integration.** As previously discussed in Section 1, we use non-medical synthetic descriptions for each image to further refine lesion localization learning. Specifically, we employ BLIP [Li et al., 2022b] which is trained on natural image datasets as our synthetic text generator to provide additional global features during training.

Given the original OCT image  $X_i$ , we generate its synthetic descriptive text and feed it into a text encoder to obtain the textual encoding feature  $F^D \in \mathbb{R}^{1 \times C^{desp}}$ . Next, we expand this feature to  $F^D \in \mathbb{R}^{H_s \times W_s \times C^{desp}}$  for subsequent fusion with visual features. This process is illustrated at the bottom left of Fig. 2. To enrich the feature representation from the primary branch with corresponding semantic information, we concatenate the visual and textual features and feed the updated feature into learnable layers, as follows:

$$F_s^{P+} = (F_s^P \oplus F^D) \mathbf{W}_s^{fuse} \quad (4)$$

To avoid disrupting the cross-attention module and to stabilize the training process, we fuse the synthetic descriptive feature with the visual feature only at the last stage,  $s = 4$ , of the primary module. In this integration, the model leverages the semantic consistency of similar lesions to enhance the visual features in regions relevant to the descriptions.

**Label-Informed Textual Guidance.** We utilize the pretrained CLIP model [Radford et al., 2021] to encode the predefined text labels for each OCT dataset, as the example shown in Fig. 1 (a). The encoded features are denoted as  $F^{clip} \in \mathbb{R}^{K \times C^{clip}}$ , where  $K$  represents the number of categories, including *background*, and  $C^{clip}$  is the dimension of the encoded features. The CLIP-encoded features are used to create similarity maps with the features generated by the visual branches. To achieve this, we need an adaptor to learn the characteristics of each lesion and align the vector dimensions.

Firstly, we generate the unified visual feature at stage  $s$  by simply adding  $Z_s^{visual} = F_s^P + F_s^T$ , and reshaping it to  $Z_s^{visual} \in \mathbb{R}^{H_s W_s \times C_s}$ . Note that the  $F_4^P$  is the  $F_4^{P+}$ , which is enhanced by synthetic text features. Then, we introduce MLP layers to transform the embeddings in the label-informed text space:

$$Z_s^{clip} = ReLU(F^{clip} \mathbf{W}_s^1) \mathbf{W}_s^2 \quad (5)$$

Where  $\mathbf{W}$  represents the learnable parameters, and  $Z_s^{clip} \in \mathbb{R}^{K \times C_s}$ . Next, we transpose the transformed CLIP feature into  $Z_s^{clip} \in \mathbb{R}^{C_s \times K}$  to align the feature dimensions for subsequent matrix operations and facilitate efficient fusion with visual feature maps. Now, we can generate the similarity map by:

$$SIM_s = r_s \times Z_s^{visual} Z_s^{clip}, \quad s \in [3, 4] \quad (6)$$

where  $r_s$  is the learnable scaling factor at stage  $s$ . The vector  $SIM_s \in \mathbb{R}^{H_s W_s \times K} \mapsto \mathbb{R}^{K \times H_s \times W_s}$  represents the similarity score between the visual features and each of the label-informed text embedding.

### 3.3 Weakly Supervised Objectives

To train the model with weak supervision and to facilitate the learning of correlations between text and visual features, we design the loss function to integrate three aspects: image-level multi-label classification, structural binary classification, and label-informed multi-label classification.

We employ the global max pooling (GMP) layer at the end of the primary encoder, followed by a convolutional layer  $\mathbf{W} \in \mathbb{R}^{C_4 \times K}$ , to generate the class prediction,  $\hat{y}_1 = \text{GMP}(F_4^{P^+})\mathbf{W}$ , and then we use the multi-label binary cross-entropy loss for training as follows:

$$\mathcal{L}_1 = -\frac{1}{K} \sum_{k=1}^K y^k \log \sigma(\hat{y}_1^k) + (1 - y^k) \log[1 - \sigma(\hat{y}_1^k)] \quad (7)$$

where  $\sigma$  is the sigmoid activation function.

For the structural encoder, which is responsible for capturing features indicating structural disruption and supporting the primary branch, we calculate the binary classification loss to distinguish between the healthy and non-healthy. For example, a multi-label target  $y$  indicating different lesions is converted to a binary label  $y_b$  (0 for healthy, 1 for lesion present). We then apply GMP followed by a convolutional layer,  $\mathbf{W} \in \mathbb{R}^{C_4 \times 2}$ , at the end of the structural encoder to obtain the binary prediction  $\hat{y}_2 = \text{GMP}(F_4^T)\mathbf{W}$ . The loss function is defined as follows:

$$\mathcal{L}_2 = -\sum_{k=1}^2 y_b^k \log(\hat{y}_2^k) \quad (8)$$

Moreover, to further enhance the model with textual guidance, we apply GMP on the obtained similarity maps to generate multi-label predictions as well. Since the SIM maps are derived from the last two stages  $s = 3, 4$ , we obtain the final label-informed predictions as follows: the class prediction from textual guidance is denoted as  $\hat{y}_3 = \text{GMP}(\text{SIM}_3)$  and  $\hat{y}_4 = \text{GMP}(\text{SIM}_4)$ , respectively. Similar to  $\mathcal{L}_1(\hat{y}_1, y)$ , we calculate the binary cross-entropy loss between the labels  $y$  and the predictions  $\hat{y}_3, \hat{y}_4$  for training, denoted as  $\mathcal{L}_3(\hat{y}_3, y)$  and  $\mathcal{L}_4(\hat{y}_4, y)$ .

Finally, we compute the weighted sum of the losses from different components of the network to define the final loss of our proposed model as follows:

$$\mathcal{L} = \lambda_1 \mathcal{L}_1 + \lambda_2 \mathcal{L}_2 + \lambda_3 \mathcal{L}_3 + \lambda_4 \mathcal{L}_4 \quad (9)$$

The  $\mathcal{L}_1$  ensures consistent localization of target regions with the enhancement from synthetic descriptions, while  $\mathcal{L}_2$  directs the model to focus on abnormal regions. The  $\mathcal{L}_3$  and  $\mathcal{L}_4$  further improve training by introducing label-informed text guidance. The effectiveness of each module is demonstrated in the experiments section.

### 3.4 Pseudo Label Generation

Once the model training is completed, we generate CAMs from different branches within the network. First, lesion CAMs are obtained from the primary branch using the learned features from the encoder's last layer, denoted as  $\mathbf{M} \in \mathbb{R}^{(K-1) \times H_4 \times W_4}$ . Additionally, similarity maps between visual and textual features from the last two stages are directly used as additional heatmaps, retaining only the lesion channels, denoted as  $\text{SIM}_s \in \mathbb{R}^{(K-1) \times H_s \times W_s}$ .

We apply the *ReLU* activation to the heatmaps, perform a weighted sum to emphasize localization, and then normalize them. Note that these maps need to be resized to the same dimensions before fusion.

$$\begin{aligned} \mathbf{M}_{fg} &= \gamma_1 \text{ReLU}(\mathbf{M}) + \gamma_3 \text{ReLU}(\text{SIM}_3) + \gamma_4 \text{ReLU}(\text{SIM}_4) \\ \mathbf{M}_{fg}^k &= \frac{\mathbf{M}_{fg}^k - \min(\mathbf{M}_{fg}^k)}{\max(\mathbf{M}_{fg}^k) - \min(\mathbf{M}_{fg}^k)} \end{aligned} \quad (10)$$

where  $k$  represents the class. Then, following common practice, we add a background map,  $\mathbf{M}_{bg}$ , by applying a threshold  $\lambda$  in the range  $[0, 1]$  to suppress the background. The final localization map is  $\mathbf{M}_{final} = \mathbf{M}_{bg} \oplus \mathbf{M}_{fg}$ . Finally, we obtain the pseudo labels for segmentation by applying *argmax* across the classes. Our training strategy is detailed in Algorithm 1.



**Algorithm 1** Training algorithm**Inputs:**  $\mathcal{D} = \{(X, y)\}^N$  -training dataset**Output:**  $PL$  - Pseudo labels $T$ - Total number of Classification Epochs $\Theta_{clip}$ - pretrained CLIP $\Theta_{blip}$ - pretrained caption generator BLIP $\mathcal{G}, \mathcal{S}$ : pretrained GAN generator and layer segmentation model

---

```

1: Initialize primary and structural encoders  $\Theta_a, \Theta_b$ 
2: Initialize cross-attention module  $\Theta_c$ 
3: Initialize synthetic description module  $\Theta_d$ 
4: Initialize adaptor  $\Theta_e$ 
5: for  $t$  in  $[1, T]$  do
6:   for every minibatch  $B$  in  $\mathcal{D}$  do
7:     Let image  $X \in B$ , and stage number is  $s$ 
8:     Calculate feature map  $F_s^P = \Theta_a(X)$  ▷ Sec. 3.1
9:     Get fake healthy image  $G = \mathcal{G}(X)$ 
10:    Get layer image  $S = \mathcal{S}(X)$ 
11:     $X' = \text{Normalize}(G + X)$  ▷ (Eq. 1)
12:    Calculate feature map  $F_s^T = \Theta_b(X')$ 
13:    Exchange features  $Z_s^P = \Theta_c^P(F_s^P, F_s^T)$  ▷ (Eq. 3)
14:    Exchange features  $Z_s^T = \Theta_c^T(F_s^T, F_s^P)$ 
15:    Get synthetic feature  $F^D = \Theta_{clip}(\Theta_{blip}(X))$  ▷ Sec. 3.2
16:    Fuse feature maps  $F_s^{P+} = \Theta_a(F_s^P \oplus F^D)$  ▷ (Eq. 4)
17:    Get label feature  $F^D = \Theta_{clip}(y)$ 
18:    Fuse visual features  $Z_s^{visual} = F_s^P + F_s^T$ 
19:    Adapt text feature  $Z_s^{clip} = \Theta_d(F^D)$  ▷ (Eq. 5)
20:    Get similarity maps  $\text{SIM}_s$ 
21:    Compute classification  $loss \mathcal{L}(\Theta_a, \Theta_b, \Theta_c)$  ▷ Sec. 3.3
22:    Compute textual guidance  $loss \mathcal{L}(\Theta_d, \Theta_e)$ 
23:    Compute gradients of  $loss$  w.r.t  $\Theta_{a-e}$ 
24:    Update  $\Theta_{a-e}$  by optimizer
25:   end for
26: end for

```

---

## 4 Dataset and Experimental Settings

### 4.1 Datasets and Evaluation Metrics

Following the AGM study [Yang et al., 2024], we evaluate our proposed method on the same three OCT B-scan datasets: RESC, Duke, and a private dataset. We employ standard evaluation metrics to assess our method’s performance, focusing on pixel-level prediction through micro-averaging mean Intersection over Union (mIoU).

### 4.2 Baselines and Evaluation Metrics

To evaluate the performance of our proposed method, we compare the quality of pseudo labels with existing WSSS methods that utilize image-level supervision. These methods include IRNet [Ahn et al., 2019], ReCAM [Chen et al., 2022a], SEAM [Wang et al., 2020b], WSMIS [Viniavskyi et al., 2020], MSCAM [Ma et al., 2020], TransWS [Zhang et al., 2022], DFP [Wang et al., 2020c], TPRO [Zhang et al., 2023], and AGM [Yang et al., 2024]. In our experiments, we consider both the base versions, for SEAM and ReCAM, and their corresponding extensions, SEAM<sup>+</sup> and ReCAM<sup>+</sup> (see Table 1). Please note that, for each method, we traverse the background threshold  $\lambda \in [0, 1]$  in increments of 0.01 using the same strategy to report the best mIoU of pseudo labels on each dataset.

In addition to assessing the final pseudo labels’ performance, we report segmentation results from networks trained on these pseudo labels in a fully supervised manner (see Table 2).

### 4.3 Implementation Details

The input images are resized to  $512 \times 512$  pixels. For visual processing, we use the pretrained MiT-b2 encoder with the first two stages frozen. The label-informed branch is encoded with CLIP-large, while the synthetic descrip-

tion branch generates text with BLIP and encodes it with CLIP-base. For all baselines and our proposed model, the threshold  $\lambda$  for final pseudo labels is selected by traversing values from 0 to 1, choosing the value that yields the best mIoU across classes on the validation set. We train the model using a learning rate of  $1 \times 10^{-4}$  with a batch size of 8 for 30 epochs, applying binary cross-entropy loss and cross-entropy loss with the Adam optimizer. Data augmentation includes random horizontal flipping, rotation, and color jittering. For semantic segmentation, we employ DeepLabV3+ [Chen et al., 2018] with a ResNet-101 backbone and Segformer with an MiT-b5 backbone, both pretrained on ImageNet [Deng et al., 2009]. All experiments are implemented with PyTorch on a single RTX A6000 GPU. The code and pretrained models are publicly available at <https://github.com/yangjiaqidig/WSSS-AGM>.

## 5 Results

### 5.1 Comparison on Pseudo Label

Table 1: Performance of pseudo labels on different datasets using our proposed method compared to previous methods. The table presents **mIoU** scores for each method. Rows indicate the performance of each method, while columns list the datasets used for evaluation along with their corresponding lesion classes, including background (bg). The best results are highlighted in bold.

Dataset		RESC				Duke			Our Dataset					
Method	Backbone	bg	SRF	PED	mIoU	bg	Fluid	mIoU	bg	SRF	IRF	EZ	HRD	mIoU
<b>Image-level supervision only - natural image.</b>														
IRNet	R50	97.78	33.75	14.66	48.73	98.10	20.45	59.27	98.18	0.01	11.29	0.07	1.17	22.14
SEAM	WR38	97.43	34.13	10.71	47.42	97.03	17.87	57.45	97.87	13.52	14.45	1.61	2.25	25.94
SEAM <sup>+</sup>	WR38	97.65	<b>47.29</b>	3.49	49.48	96.75	18.64	57.69	97.95	13.30	14.68	1.71	2.29	25.99
ReCAM	R101	97.66	14.23	19.11	43.67	96.41	11.67	54.04	97.13	0.10	9.42	1.02	1.54	21.84
ReCAM <sup>+</sup>	R101	97.96	12.71	36.99	49.22	96.87	13.86	55.37	97.47	1.01	9.21	0.68	0.72	21.82
<b>Image-level supervision only - medical image.</b>														
WSMIS	R101	95.64	24.64	2.96	41.08	96.41	0.42	48.41	<b>98.57</b>	26.71	8.93	0.08	0.17	26.89
MSCAM	R101	97.25	10.14	11.97	39.79	98.00	17.98	57.99	97.36	22.50	1.47	<b>3.25</b>	0.14	24.94
TransWS	MiT	98.18	34.88	17.22	50.09	98.15	27.01	62.58	97.52	9.41	11.21	0.11	1.96	24.04
DFP	R101	97.72	6.40	15.64	39.92	98.24	15.14	56.69	98.31	18.05	10.06	0.67	<b>5.72</b>	26.56
AGM	R50	98.34	43.94	22.33	54.87	98.29	30.06	64.17	97.09	31.76	11.17	1.74	0.57	28.46
<b>Image-level supervision + text - multimodal.</b>														
TPRO	MiT	97.10	30.41	8.27	45.26	97.72	27.80	62.76	95.80	11.03	13.37	0.18	0.85	24.25
<b>Ours</b>	MiT	<b>98.60</b>	43.50	<b>41.35</b>	<b>61.15</b>	<b>98.47</b>	<b>37.74</b>	<b>68.11</b>	98.40	<b>33.46</b>	<b>20.40</b>	1.15	1.84	<b>31.05</b>

Since our model is designed to generate high-quality CAMs for better pseudo labels, we assess pseudo label performance in this section. The results in Table 1 compare the pseudo labels generated by our method and the baselines against the pixel-level ground truth on the validation set. Due to the limited availability of pixel-level annotations, we use the validation set as the final evaluation metric. To ensure a fair comparison, we report the highest scores achieved by each baseline and our method on the validation set. Each dataset includes the background class (*bg*) and various lesion classes: Subretinal Fluid (*SRF*) and Pigment Epithelial Detachment (*PED*) for RESC; *Fluid* for Duke; and *SRF*, Intraretinal Fluid (*IRF*), Ellipsoid Zone disruption (*EZ*), and Hyperreflective Dots (*HRD*) for our dataset. The mIoU is calculated across all classes within each dataset. To facilitate analysis, the methods are organized into three categories based on the data domain and modality: (1) image-level supervision designed for natural images, (2) image-level supervision designed for medical images, and (3) image-level supervision combined with textual information (multimodal).

Our proposed method demonstrates superior performance across three datasets, achieving higher mIoU scores compared to other WSSS methods. However, as noted in AGM [Yang et al., 2024], applying the same threshold across different lesions’ CAMs leads to an inherent trade-off, so high overall mIoU may not guarantee optimal performance for each lesion class. On the RESC dataset, our method significantly outperforms the second-best method, AGM, achieving overall mIoU of **61.15%** compared to 54.87%. Specifically, for segmentation in the *PED* lesion, our method attains an IoU of **41.35%**, nearly double AGM’s 22.33%. This substantial improvement indicates our method’s effectiveness in accurately relatively challenging lesions. Although AGM performs slightly better on the *SRF* lesion (43.94% vs.

43.50%), our method demonstrates consistently strong and balanced performance across both lesion classes, resulting in a higher overall performance.

In the Duke dataset, which contains only the *Fluid* lesion class, our method achieves a mIoU of **68.11%**, outperforming AGM by 3.94% and TPRO by 5.35%. Specifically, our method attains an IoU of 37.74% for the *Fluid* class, surpassing AGM’s 30.06% by 7.68%.

Our private dataset presents the most challenging scenario due to the presence of four different lesion types, some with subtle features and sparse pixel representation. Despite these challenges, our method achieves the highest mIoU of **31.05%**, outperforming AGM by 2.59%. It excels in segmenting the *SRF* and *IRF* classes, achieving IoUs of 33.46% and 20.40%, respectively, surpassing AGM by 1.70% and 9.23%. Other methods like DFP and MSCAM achieve higher IoUs in certain classes, such as *HRD* and *EZ*, but they do so by sacrificing accuracy in other lesion types largely. For instance, MSCAM attains a higher IoU in *EZ* (3.25%), but its performance in *IRF* drops significantly to only 1.47%, whereas our method achieves 20.40% in *IRF*.

These findings indicate that our method not only achieves high overall mIoU scores but also maintains balanced performance across different lesion classes. Interestingly, TPRO, which also utilizes textual information, sometimes performs worse than methods relying solely on image data. One possible explanation is that TPRO generates CAMs using features from earlier network stages, which are less specific and struggle to capture the relatively small target regions in OCT images, unlike the larger regions in the histopathology images used by TPRO. Besides, while both TPRO and our method utilize textual information, TPRO uses only label text and shared knowledge text across the entire dataset, which may not provide sufficient independent, image-specific information. In contrast, our method leverages per-image independent text, allowing for a more tailored and detailed semantic understanding of each image, as detailed in Section 5.3.

## 5.2 Comparison on Semantic Segmentation Results

Pseudo labels generated with a WSSS model can be used as ground truth to train a separate semantic segmentation model. To provide a comprehensive comparison of the segmentation task, we select SEAM<sup>+</sup>, AGM, and TPRO from different paradigms (see Table 1) and compare their mIoU performance with our proposed method, all trained using their respective pseudo labels. The results are presented on the RESC and Duke datasets using DeepLabV3+ (ResNet-50/101) and Segformer architectures as shown in Table 2. The *Upper Bound* represents the performance achieved when using pixel-level ground truth for training. Since the Duke dataset lacks pixel-level annotations, its *Upper Bound* is marked as ‘-’. Notably, Segformer (b5) achieves the highest upper-bound performance at 77.1%.

Table 2: Comparison of segmentation results (mIoU) between our proposed method, SEAM<sup>+</sup> from the computer vision domain, AGM from the OCT domain, and TPRO from a CLIP-based strategy, on the RESC and Duke datasets. The comparison uses DeepLabV3+ (ResNet-50/101) and Segformer. The best results are in **bold**. For reference, the *Upper Bound* represents a fully supervised segmentation method using pixel-level ground truth with various models.

Segmentation Model		RESC	Duke
<i>Upper Bound</i>	U-Net	67.75	-
	DeepLabV3+ (ResNet-101)	<b>71.65</b>	-
	Segformer (b2)	71.75	-
	Segformer (b5)	<b>77.10</b>	-
SEAM <sup>+</sup>	DeepLabV3+ (ResNet-50)	49.24	58.28
	DeepLabV3+ (ResNet-101)	49.62	59.50
AGM	DeepLabV3+ (ResNet-50)	52.11	66.26
	DeepLabV3+ (ResNet-101)	53.87	66.42
TPRO	DeepLabV3+ (ResNet-101)	47.86	64.23
	Segformer (b5)	47.76	64.90
<b>Ours</b>	DeepLabV3+ (ResNet-101)	59.68	<b>71.07</b>
	Segformer (b5)	<b>60.52</b>	70.65

Compared to other WSSS approaches, our method consistently demonstrates superior performance on both datasets, largely due to the higher quality pseudo labels generated by our model (see Table 1), leading to a more accurate segmentation model. Since DeepLabV3+ with ResNet-101 has shown stronger performance than ResNet-50, and Segformer (b5) performed exceptionally well in the *Upper Bound* evaluation, we report results using ResNet-101 and Segformer (b5) for both TPRO and ours. On the RESC dataset, our method achieves 60.52% mIoU with Segformer (b5) and 71.07% mIoU with DeepLabV3+ (ResNet-101) on the Duke dataset, outperforming the other models by at least 6% and 4%, respectively. Interestingly, Segformer (b5), when trained on generated pseudo labels, does not

significantly outperform DeepLabV3+ as observed in the *Upper Bound* and even performs worse on the Duke dataset. This indicates that the generated pseudo labels still lack the quality of true ground truth, particularly in capturing finer, more precise details.

### 5.3 Ablation Studies

In this section, we comprehensively evaluate our proposed model. To ensure unbiased results, all experiments are run five times, and we report the highest value unless specified.

**Effect of Different Module:** In Table 3, we assess the impact of each sub-module in our proposed method on two public datasets, focusing on the performance of pseudo labels measured by overall mIoU scores across lesions. As discussed in Section 3.1, the *base* denotes the primary image branch that processes the original image as input, while the *layer* and *anomaly* refer to the inputs for the structural branch. Additionally, the *clip* and *caption* represent the two modules from the textual branch, as outlined in Section 3.2, providing label-informed guidance and synthetic descriptions. Note that the *clip* used is CLIP-large, and the *caption* is generated by BLIP and encoded into vectors by CLIP-base.

Table 3: Ablation study for our proposed method on public datasets (mIoU). Roman numerals in the first column correspond to different combinations of these components, as detailed in the rows.

	base	layer	anomaly	clip	caption	RESC	Duke
I	✓					52.09	64.57
II	✓	✓				55.38	65.66
III	✓		✓			55.24	65.91
IV	✓			✓		54.18	66.88
V	✓				✓	51.58	66.28
VI	✓	✓	✓	✓		55.26	65.55
VII	✓	✓		✓	✓	57.68	66.62
VIII	✓		✓	✓	✓	58.70	65.15
IX	✓	✓	✓	✓	✓	<b>61.15</b>	<b>68.11</b>

As shown in Table 3, the performance generally increases with the addition of sub-modules, reaching its peak with the full architecture IX (61.15% and 68.11% on the RESC and Duke datasets, respectively). However, we observe some interesting performance drops when adding certain sub-modules, such as VI vs II on both datasets, V vs I on the RESC dataset, and VIII on the Duke dataset. These inconsistencies can be attributed to several factors: 1) The full model (IX) benefits from a synergistic effect, where all sub-modules complement each other, resulting in more stable and higher performance. In contrast, partial combinations may disrupt this balance and fail to fully leverage the model’s potential. 2) Since we report the highest values in the table, the variance in performance for smaller sub-module combinations may be larger, making some simpler combinations appear better, despite the overall structure with more modules being more consistent. We will explore this variance in the following section.

**CAM Variation Analysis:** As mentioned above, while we focus on the highest values for comparison, the inherent variability in CAM generation can lead to fluctuations in stability across runs. This section examines the variations to ensure that peak scores are not simply due to chance or “lucky outcomes”. In Table 4, we present the mean, standard deviation, and the highest and lowest performance across five runs for each experiment, referencing the configurations in Table 3 to provide a clearer view of stability on the RESC dataset. Notably, partial configurations, such as II, show lower stability, with a minimum performance of 32.61%, in contrast to VI, which achieves comparable top performance but exhibits less variation overall. The complete architecture (IX) consistently yields the best performance with relatively low variation, even in its lowest-scoring run.

**Label-Informed Features:** Table 5 presents the performance of pseudo labels on the RESC dataset when using different label text encodings: Random vectors, MedCLIP<sup>3</sup>, CLIP-base, and CLIP-large. For this study, we used a simplified model structure consisting only of the primary branch with the CLIP label-informed branch to isolate and examine the effect of each encoding method. The *Random* serves as a baseline, allowing us to assess how much each specific label encoding improves performance over a non-informative input.

The results indicate that CLIP-based encodings outperform both MedCLIP and the Random baseline, demonstrating better stability and higher performance. Interestingly, MedCLIP does not surpass Random, with a lower mean mIoU (47.46%) and higher variability. This suggests that MedCLIP, fine-tuned on radiology images rather than a large

<sup>3</sup><https://github.com/Kaushalya/medclip>

Table 4: Mean, standard deviation (Std), highest, and lowest mIoU performance (%) over five runs for each configuration on the RESC dataset, illustrating the stability of different sub-module combinations. The highest values are in **bold**, and the largest variation is highlighted in **red**.

	Mean (%)	Std	High (%)	Low (%)
I	49.75	$\pm 1.72$	52.09	47.20
II	46.91	<b><math>\pm 8.74</math></b>	55.38	<b>32.61</b>
V	49.90	$\pm 1.07$	51.58	48.34
VI	52.10	$\pm 2.24$	55.26	49.56
VIII	53.53	$\pm 2.80$	58.70	51.01
IX	<b>56.87</b>	$\pm 2.54$	<b>61.15</b>	<b>54.33</b>

variety of medical images, may lack foundational text-image relationships needed for effective label alignment with OCT images. This finding highlights the value of general-purpose CLIP encodings, which retain a broad semantic understanding that proves advantageous even in OCT-specific applications.

Table 5: Comparison of model performance on the RESC dataset using different label text encodings: Random vectors, MedCLIP, CLIP-base, and CLIP-large. For each encoding method, the table reports the mean, standard deviation (Std), highest, and lowest mIoU scores over five runs, highlighting the impact of each encoding on performance and stability.

	Mean (%)	Std	High (%)	Low (%)
Random	49.94	$\pm 1.23$	51.26	47.94
MedCLIP	47.46	$\pm 2.36$	52.11	45.55
CLIP-base	52.36	$\pm 2.36$	54.63	48.38
CLIP-large	51.32	$\pm 1.98$	54.18	49.44

We examine the impact of combining CLIP features with visual features from different encoder stages, as shown in Table 6. The stage selection for SIM generation aligns with the included loss terms, as illustrated in Fig. 2; for example, if  $\mathcal{L}_3$  is included, the SIM map from Stage 3 is used. Loss terms  $\mathcal{L}_1$ ,  $\mathcal{L}_2$ ,  $\mathcal{L}_3$ , and  $\mathcal{L}_4$  are defined in Eq. (9). We can observe that raw CAM generated solely from the primary branch is insufficient, yielding a mean mIoU of 49.75%. However, adding structural information to visual features effectively improves the performance (see row 2). As shown in row 3 of Table 6, using only Stage 4 features with CLIP lowers mean performance to 45.85% and reduces stability, suggesting that these abstract features lack fine-grained details required for precise lesion identification. By contrast, combining features from the last two stages ( $\mathcal{L}_3 + \mathcal{L}_4$ ) in row 4 achieves the highest stability and performance, indicating that mid-level features from Stage 3 provide complementary spatial details that enhance the final output.

Table 6: Ablation study on different loss configurations on the RESC dataset. The loss terms  $\mathcal{L}_1$ ,  $\mathcal{L}_2$ ,  $\mathcal{L}_3$ , and  $\mathcal{L}_4$  are defined in Eq. (9). Mean, standard deviation (Std), highest, and lowest mIoU scores are reported over five runs. The best results are highlighted in **bold**.

Controller	Mean(%)	Std	High(%)	Low (%)
$\mathcal{L}_1$	49.75	$\pm 1.72$	52.09	47.20
$\mathcal{L}_1 + \mathcal{L}_2$	51.89	$\pm 0.95$	53.11	50.71
$\mathcal{L}_1 + \mathcal{L}_2 + \mathcal{L}_4$	45.85	$\pm 5.88$	53.40	39.14
$\mathcal{L}_1 + \mathcal{L}_2 + \mathcal{L}_3 + \mathcal{L}_4$	<b>56.87</b>	$\pm 2.54$	<b>61.15</b>	<b>54.33</b>

**Synthetic Description Analysis:** Table 7 presents the performance (mIoU) of pseudo labels generated using different synthetic description methods (ViT-GPT2<sup>4</sup> and BLIP). We experiment with three encoders—MiniLM-L12-v2 [Reimers, 2019], CLIP-large, and CLIP-base—to convert the descriptions into vector space, with dense vector dimensions of 384, 512, and 768, respectively. We observe that BLIP with the CLIP-base encoder yields the best performance, while ViT-GPT generally underperforms compared to BLIP, and MiniLM-L12-v2 encoding also shows overall lower effectiveness than the CLIP encoders. Why do we observe this pattern, and how does non-medical description guide model learning? This question warrants further exploration, and Fig. 5 and Fig. 6 provide insights into a potential underlying cause.

<sup>4</sup><https://huggingface.co/nlpconnect/vit-gpt2-image-captioning>

Table 7: Ablation study on synthetic description methods, comparing mIoU performance (%) of different text models (ViT-GPT2 and BLIP) with various text encoders (CLIP-base, CLIP-large, and MiniLM-L12-v2) for embedding text into vector space.

	Text Encoders		
	MiniLM-L12-v2	CLIP-large	CLIP-base
ViT-GPT2	55.29	55.61	54.98
BLIP	55.66	56.94	<b>61.15</b>

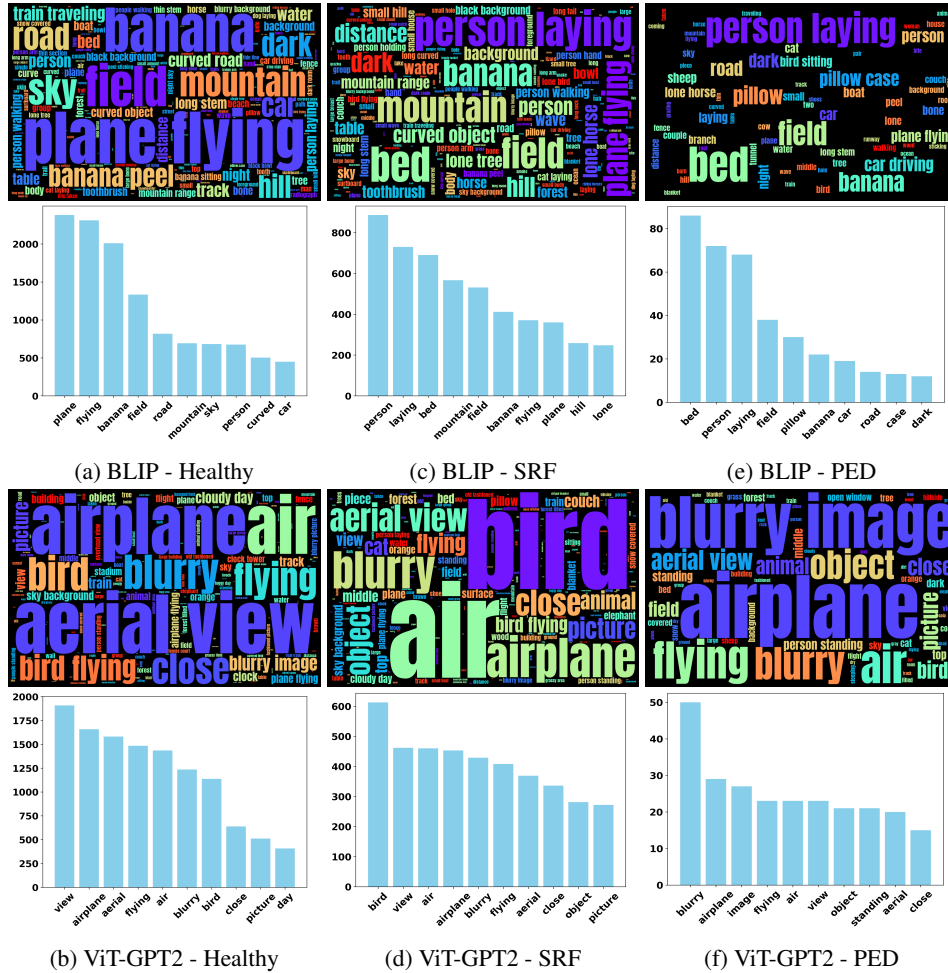


Figure 5: Visualization of common descriptions for each condition in the RESC dataset, displayed as word clouds and histograms of common word distributions. (a) and (b) show results for the healthy image collection using BLIP and ViT-GPT2 text generators, respectively. Similarly, (c) and (d) represent the SRF lesion collection, while (e) and (f) display the PED lesion collection for the two generators.

From the text generator perspective, as shown in Fig. 5, BLIP generates more informative descriptions compared to ViT-GPT2. For example, BLIP includes a wider variety of relevant phrases such as “*person laying*,” “*pillow case*,” and “*curved*”, while ViT-GPT2 frequently outputs less relevant terms like “*aerial view*,” “*blurry*,” and “*picture*”. This explains why BLIP is more effective than ViT-GPT2, as shown in Table 7, due to BLIP’s more accurate and meaningful descriptions of the global context and relationships between objects in the images. On the other hand, from the perspective of descriptions within the same generator across different lesion types, we observe differences in word choices between lesion sets. For instance, healthy images often include terms like “*plane*” and “*flying*,” while SRF lesion descriptions feature “*person*” and “*hill*,” and PED lesions commonly include “*pillow*” and “*bed*.” Certain high-frequency words reflect the overall retinal structure, as expected, and capture the general retinal shape. This

supports the effectiveness of non-medical descriptions in guiding the model to distinguish between lesions through descriptive variation.

To further assess the consistency of synthetic descriptions for OCT images, we analyze similarity scores among their text embeddings. Similar 2D retinal OCT images, such as adjacent slices within a 3D volume, are expected to have consistent visual context; therefore, we anticipate that text generated for similar images will also be consistent. Fig. 6 shows cosine similarity scores across sliding window sizes (ranging from 3 to 65) for BLIP and ViT-GPT2 text embeddings within the RESC dataset’s 3D OCT volumes. Higher similarity scores are expected for smaller window sizes, decreasing as more distant slices are included. Each score represents the average similarity between neighboring slices and the central target slice within the window. The results indicate that BLIP achieves higher similarity scores than ViT-GPT2, reflecting stronger contextual consistency. Additionally, CLIP-base encoding yields the highest similarity scores among the encoders, aligning with the superior pseudo-label mIoU observed for BLIP with CLIP-base in Table 7. These findings underscore the value of synthetic non-medical text, as its consistent descriptions of the OCT domain enhance model performance.

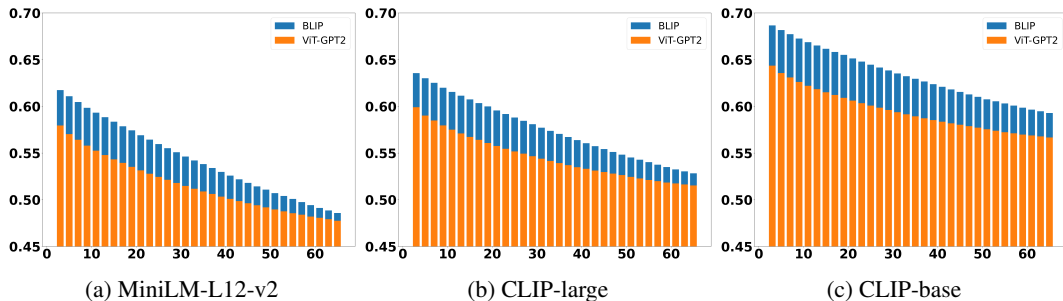


Figure 6: Similarity score histograms for text embeddings generated by BLIP (blue) and ViT-GPT2 (orange) within OCT 3D volumes on the RESC dataset, encoded with (a) MiniLM-L12-v2, (b) CLIP-large, and (c) CLIP-base. Each shows cosine similarity scores across sliding window sizes, with the x-axis representing window size and the y-axis displaying similarity scores. Note that blue bars represent only the visible portion extending above the orange bars.

**Backbone Analysis:** To evaluate backbone size and stage-freezing strategy, we present the performance of different MiT sizes and frozen stages in Table 8. Fully fine-tuning all parameters leads to instability and poorer performance on OCT images, as seen with MiT-b2 in the first row, which shows high variance and a mean mIoU of only 52.33%. This suggests that freezing early stages effectively leverages pretrained feature representations and stabilizes training. MiT-b1 (\* S1+S2), being smaller, reaches only a peak mIoU of 55.76%. In contrast, the large MiT-b5 (\* S1+S2), while powerful, is overly heavy and potentially limits the contribution of other modules. Although further tuning could benefit MiT-b5, it remains less efficient in our current setup. Balancing efficiency and performance, we select MiT-b2 (\* S1+S2) for our final design.

Table 8: Ablation study on the RESC dataset using different sizes of pretrained MiT backbones in our proposed method. S1 and S2 denote stages 1 and 2 in MiT, respectively, and \* indicates which stages are frozen. We report the mean, standard deviation, highest, and lowest mIoU scores over five runs, along with the number of trainable parameters (in millions). Best results are in **bold**.

	Mean (%)	Std	High (%)	Low (%)	Params (M)
MiT-b2	52.33	±5.10	58.55	43.23	54.1
MiT-b2 (* S1)	51.34	±3.25	55.85	47.33	48.3
MiT-b2 (* S1+S2)	<b>56.87</b>	±2.54	<b>61.15</b>	<b>54.33</b>	44.6
MiT-b1 (* S1+S2)	54.00	±2.16	55.76	49.83	25.0
MiT-b5 (* S1+S2)	52.54	±3.24	57.77	48.00	157.2

## 5.4 Qualitative Results

In Fig. 7, we present several examples comparing the pseudo labels generated by our proposed method to those from other baseline techniques. Our method achieves more accurate localization while minimizing incorrect predictions in irrelevant areas. In contrast, the baseline methods exhibit less stability across images. For example, ReCAM often produces overly sensitive predictions, such as focusing on edge regions for SRF (row 1) or generating misaligned predictions (rows 2 and 5). Similarly, TPRO often highlights irrelevant regions, as evident in its broader false positive

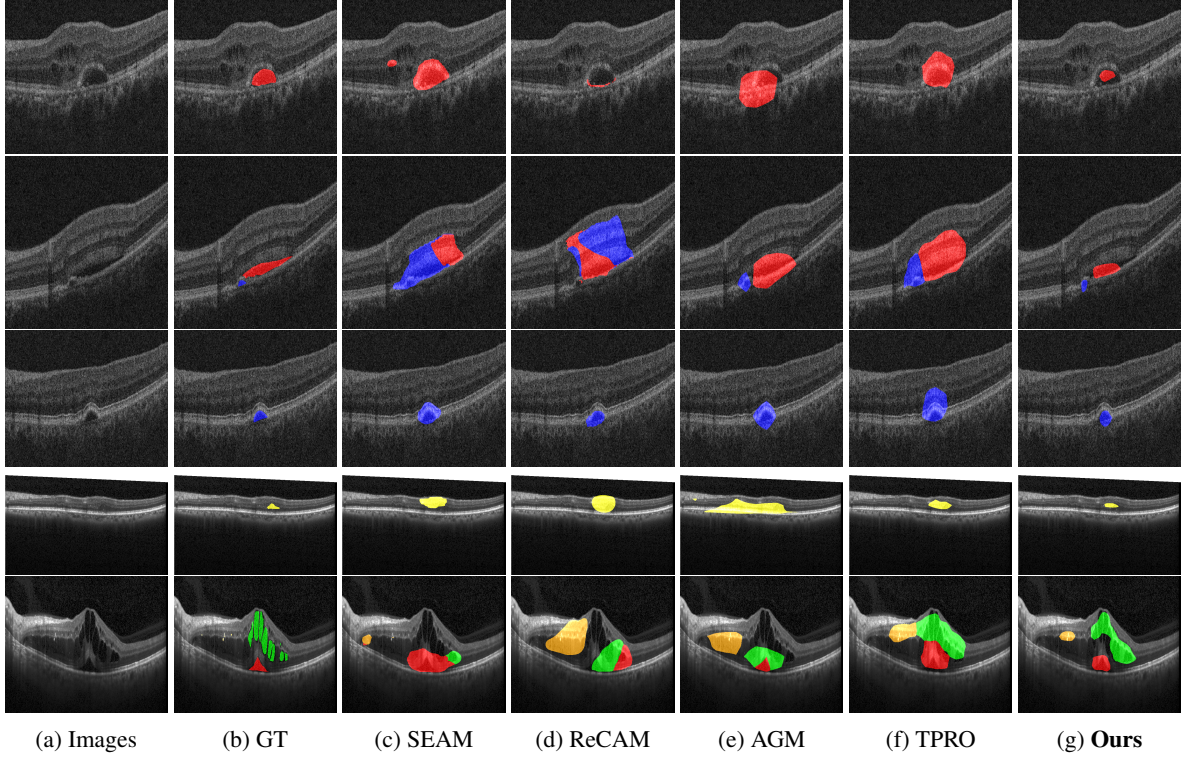


Figure 7: Qualitative visualization of pseudo labels generated by baselines and our method on three validation sets. Each row presents a sample with ground truth shown in the second column. Pseudo labels are overlaid on the original images for clarity, with lesion colors as follows: red (SRF), blue (PED), yellow (Fluid), orange (HRD), and green (IRF)

coverage compared to our method. The closer alignment of our pseudo labels with the ground truth masks highlights the superior effectiveness of our approach in generating accurate and reliable predictions.

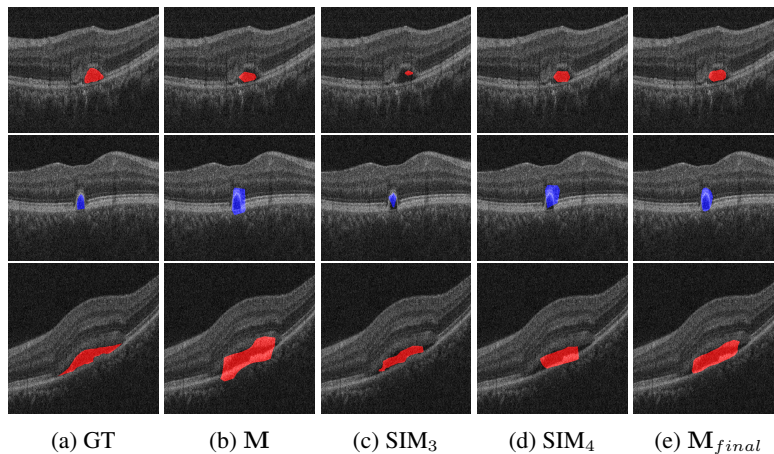


Figure 8: Visualization of pseudo labels generated from different sources of CAMs. (a) GT represents the ground truth, (b) M corresponds to the primary branch output, (c)  $SIM_3$  is the similarity map between visual and textual features from stage 3, (d)  $SIM_4$  is the similarity map from stage 4, and (e)  $M_{final}$  represents the proposed combined result integrating the three sources.

We present the mIoU performance for different sources of CAMs in Table 6. To further illustrate the impact of our proposed three sources of CAMs, we provide examples of the generated pseudo labels overlaid on the original OCT images in Fig. 8. The pseudo labels generated by M,  $SIM_3$ ,  $SIM_4$ , and  $M_{final}$  are described in Eq. (10). We can



observe that  $SIM_3$  is relatively more conservative to smaller regions compared to  $SIM_4$ , which makes sense as it is derived from the early stage of the network, where the features primarily capture low-level details and localized patterns. The results generated by the primary branch,  $M$ , demonstrate its stable capability to capture lesions. When combined with  $SIM_3$  and  $SIM_4$ , our final proposed  $M_{final}$  benefits from the complementary focus of all three sources, producing more stable and accurate results compared to the ground truth.

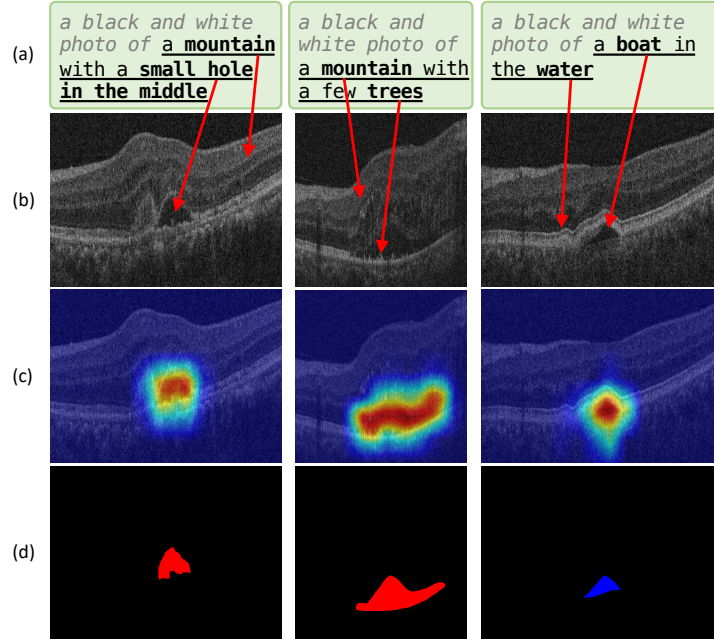


Figure 9: Visualization of three examples of CAMs generated by our model with synthetic descriptions on the RESC dataset. Each example consists of: (a) synthetic descriptive text; (b) the original OCT image; (c) CAMs generated by our model; and (d) the ground truth lesion mask for comparison. Red arrows indicate areas in the OCT image that potentially correspond to highlighted keywords in the text.

In Fig. 9, we present three examples from the RESC dataset, each with synthetic text generated by BLIP and corresponding CAMs produced by our proposed method. Each description begins with the prefix “a black and white photo of,” followed by the generated description, which provides a global perspective that leverages non-medical language to convey meaningful information about object relationships and relative positions. By comparing the text and visuals, we can observe that these non-medical descriptions offer effective cues for lesion localization. Red arrows indicate the regions in the OCT image that potentially correspond to key phrases in the synthetic text. For instance, in the first column of (a), the phrase “a small hole in the middle” suggests the relative location of the lesion, which aligns well with the position of the SRF lesion. As shown in (c), our model accurately localizes the lesions with high confidence, demonstrating its effectiveness in integrating these textual features.

## 6 Discussion and Conclusion

In this paper, we propose a novel method for OCT lesion segmentation under a weakly supervised setting, using only image-level labels as supervision. Our approach leverages imperfect yet effective information to improve pseudo-label quality and enhance segmentation results. We incorporate structural information to capture potential relationships between certain lesions and their typical layer patterns. Meanwhile, synthetic textual data generated by non-medical pretrained models provides consistent global context, strengthening model robustness. Furthermore, label-informed textual features contribute a lesion-specific local perspective, further refining segmentation accuracy. We validated the effectiveness of our method across three OCT datasets, supported by comprehensive ablation studies examining the contribution of each module. Our approach establishes a new state-of-the-art, outperforming other baselines in weakly supervised lesion segmentation on retinal OCT images.

By incorporating synthetic descriptions generated from non-medical pretrained models, our method effectively leverages existing large-scale vision-language models to enhance segmentation performance. Although these models may introduce some noise due to the lack of alignment with medical-specific features, we have maximized their benefits by

successfully integrating textual information into medical imaging analysis. This success presents an opportunity for further improvement: utilizing domain-specific models or incorporating medical reports could provide more specialized guidance and potentially enhance performance even further.

In terms of generalization to other non-OCT modalities, the structural branch relying on features unique to OCT images, such as layer segmentation, can limit the applicability to other types of medical imaging. However, the other components of our model, such as the use of cross-domain foundation models for supplemental textual information, can be readily adopted for various medical imaging modalities to exploit the information embedded in vision-language data.

In conclusion, we have demonstrated that leveraging structural, synthetic, and label-informed features significantly improves weakly supervised OCT lesion segmentation. Our findings validate the feasibility of incorporating textual information in OCT analysis and suggest the potential for integrating domain-specific descriptions in future work. We believe this approach presents a promising opportunity to reduce the need for extensive manual annotation through weakly supervised methods, while effectively leveraging multi-source information to strengthen model performance and support clinical decision-making.

## Acknowledgments

This work was partially supported by grants PSC-CUNY Research Award 65406-00 53, NSF CCF-2144901, and NIH R21CA258493.

## References

- Ursula Schmidt-Erfurth, Gregor S Reiter, Sophie Riedl, Philipp Seeböck, Wolf-Dieter Vogl, Barbara A Blodi, Amitha Domalpally, Amani Fawzi, Yali Jia, David Sarraf, et al. Ai-based monitoring of retinal fluid in disease activity and under therapy. *Progress in retinal and eye research*, page 100972, 2021.
- Pedro O Pinheiro and Ronan Collobert. Weakly supervised semantic segmentation with convolutional networks. In *CVPR*, page 6, 2015.
- Jiwoon Ahn and Suha Kwak. Learning pixel-level semantic affinity with image-level supervision for weakly supervised semantic segmentation. In *CVPR*, pages 4981–4990, 2018.
- Alexander Kolesnikov and Christoph H Lampert. Seed, expand and constrain: Three principles for weakly-supervised image segmentation. In *ECCV*, pages 695–711, 2016.
- Suha Kwak, Seunghoon Hong, and Bohyung Han. Weakly supervised semantic segmentation using superpixel pooling network. In *AAAI*, 2017.
- Sijie Niu, Ruiwen Xing, Xizhan Gao, Tingting Liu, and Yuehui Chen. A fine-to-coarse-to-fine weakly supervised framework for volumetric sd-oct image segmentation. *IET Computer Vision*, pages 123–134, 2023.
- Di Lin, Jifeng Dai, Jiaya Jia, Kaiming He, and Jian Sun. Scribblesup: Scribble-supervised convolutional networks for semantic segmentation. In *CVPR*, pages 3159–3167, 2016.
- Paul Vernaza and Manmohan Chandraker. Learning random-walk label propagation for weakly-supervised semantic segmentation. In *CVPR*, pages 7158–7166, 2017.
- Xiangde Luo, Minhao Hu, Wenjun Liao, Shuwei Zhai, Tao Song, Guotai Wang, and Shaoting Zhang. Scribble-supervised medical image segmentation via dual-branch network and dynamically mixed pseudo labels supervision. *arXiv preprint arXiv:2203.02106*, pages 528–538, 2022.
- Gabriele Valvano, Andrea Leo, and Sotirios A Tsafaris. Self-supervised multi-scale consistency for weakly supervised segmentation learning. In *DART*, pages 14–24, 2021.
- Tianqi Ma, Qilong Wang, Hongzhi Zhang, and Wangmeng Zuo. Delving deeper into pixel prior for box-supervised semantic segmentation. *TIP*, pages 1406–1417, 2022.
- Youngmin Oh, Beomjun Kim, and Bumsub Ham. Background-aware pooling and noise-aware loss for weakly-supervised semantic segmentation. In *CVPR*, pages 6913–6922, 2021.
- Jifeng Dai, Kaiming He, and Jian Sun. Boxsup: Exploiting bounding boxes to supervise convolutional networks for semantic segmentation. In *ICCV*, pages 1635–1643, 2015.
- Hoel Kervadec, Jose Dolz, Meng Tang, Eric Granger, Yuri Boykov, and Ismail Ben Ayed. Constrained-cnn losses for weakly supervised segmentation. *MedIA*, pages 88–99, 2019.

- Bolei Zhou, Aditya Khosla, Agata Lapedriza, Aude Oliva, and Antonio Torralba. Learning deep features for discriminative localization. In *CVPR*, pages 2921–2929, 2016.
- Yuqi Lin, Minghao Chen, Wenxiao Wang, Boxi Wu, Ke Li, Binbin Lin, Haifeng Liu, and Xiaofei He. Clip is also an efficient segmenter: A text-driven approach for weakly supervised semantic segmentation. In *Proceedings of the IEEE/CVF Conference on Computer Vision and Pattern Recognition*, pages 15305–15314, 2023.
- Songhe Deng, Wei Zhuo, Jinheng Xie, and Linlin Shen. Question-answer cross language image matching for weakly supervised semantic segmentation. *arXiv preprint arXiv:2401.09883*, 2024.
- Zifeng Wang, Zhenbang Wu, Dinesh Agarwal, and Jimeng Sun. Medclip: Contrastive learning from unpaired medical images and text. *arXiv preprint arXiv:2210.10163*, 2022.
- Ramprasaath R Selvaraju, Michael Cogswell, Abhishek Das, Ramakrishna Vedantam, Devi Parikh, and Dhruv Batra. Grad-cam: Visual explanations from deep networks via gradient-based localization. In *ICCV*, pages 618–626, 2017.
- Haofan Wang, Zifan Wang, Mengnan Du, Fan Yang, Zijian Zhang, Sirui Ding, Piotr Mardziel, and Xia Hu. Score-cam: Score-weighted visual explanations for convolutional neural networks. In *CVPR*, pages 24–25, 2020a.
- Harish Guruprasad Ramaswamy et al. Ablation-cam: Visual explanations for deep convolutional network via gradient-free localization. In *WACV*, pages 983–991, 2020.
- Beomyoung Kim, Sangeun Han, and Junmo Kim. Discriminative region suppression for weakly-supervised semantic segmentation. In *AAAI*, pages 1754–1761, 2021.
- Yude Wang, Jie Zhang, Meina Kan, Shiguang Shan, and Xilin Chen. Self-supervised equivariant attention mechanism for weakly supervised semantic segmentation. In *CVPR*, pages 12275–12284, 2020b.
- Lixiang Ru, Yibing Zhan, Baosheng Yu, and Bo Du. Learning affinity from attention: End-to-end weakly-supervised semantic segmentation with transformers. In *CVPR*, pages 16846–16855, 2022.
- Zhaozheng Chen, Tan Wang, Xiongwei Wu, Xian-Sheng Hua, Hanwang Zhang, and Qianru Sun. Class re-activation maps for weakly-supervised semantic segmentation. In *CVPR*, pages 969–978, 2022a.
- Xiangwei Shi, Seyran Khademi, Yunqiang Li, and Jan van Gemert. Zoom-cam: Generating fine-grained pixel annotations from image labels. In *ICPR*, pages 10289–10296, 2021.
- Jinheng Xie, Jianfeng Xiang, Junliang Chen, Xianxu Hou, Xiaodong Zhao, and Linlin Shen. C2am: Contrastive learning of class-agnostic activation map for weakly supervised object localization and semantic segmentation. In *Proceedings of the IEEE/CVF Conference on Computer Vision and Pattern Recognition*, pages 989–998, 2022a.
- Seungho Lee, Minhyun Lee, Jongwuk Lee, and Hyunjung Shim. Railroad is not a train: Saliency as pseudo-pixel supervision for weakly supervised semantic segmentation. In *Proceedings of the IEEE/CVF conference on computer vision and pattern recognition*, pages 5495–5505, 2021.
- Tong Wu, Junshi Huang, Guangyu Gao, Xiaoming Wei, Xiaolin Wei, Xuan Luo, and Chi Harold Liu. Embedded discriminative attention mechanism for weakly supervised semantic segmentation. In *CVPR*, pages 16765–16774, 2021.
- Junsuk Choe, Seungho Lee, and Hyunjung Shim. Attention-based dropout layer for weakly supervised single object localization and semantic segmentation. *TPAMI*, pages 4256–4271, 2020.
- Sanghyun Jo and In-Jae Yu. Puzzle-cam: Improved localization via matching partial and full features. In *ICIP*, pages 639–643, 2021.
- Liang-Chieh Chen, George Papandreou, Iasonas Kokkinos, Kevin Murphy, and Alan L Yuille. Deeplab: Semantic image segmentation with deep convolutional nets, atrous convolution, and fully connected crfs. *IEEE transactions on pattern analysis and machine intelligence*, 40(4):834–848, 2017a.
- Liang-Chieh Chen, George Papandreou, Florian Schroff, and Hartwig Adam. Rethinking atrous convolution for semantic image segmentation. *arXiv preprint arXiv:1706.05587*, 2017b.
- Holger R Roth, Dong Yang, Ziyue Xu, Xiaosong Wang, and Daguang Xu. Going to extremes: weakly supervised medical image segmentation. *Machine Learning and Knowledge Extraction*, pages 507–524, 2021.
- Jing Wang, Wanyue Li, Yiwei Chen, Wangyi Fang, Wen Kong, Yi He, and Guohua Shi. Weakly supervised anomaly segmentation in retinal oct images using an adversarial learning approach. *Biomedical optics express*, pages 4713–4729, 2021.
- Gaurav Patel and Jose Dolz. Weakly supervised segmentation with cross-modality equivariant constraints. *MedIA*, page 102374, 2022.

- Xi Ouyang, Zhong Xue, Yiqiang Zhan, Xiang Sean Zhou, Qingfeng Wang, Ying Zhou, Qian Wang, and Jie-Zhi Cheng. Weakly supervised segmentation framework with uncertainty: A study on pneumothorax segmentation in chest x-ray. In *MICCAI*, pages 613–621, 2019.
- Ostap Viniavskiy, Mariia Dobko, and Oles Dobosevych. Weakly-supervised segmentation for disease localization in chest x-ray images. In *AIME*, pages 249–259, 2020.
- Soufiane Belharbi, Jérôme Rony, Jose Dolz, Ismail Ben Ayed, Luke McCaffrey, and Eric Granger. Deep interpretable classification and weakly-supervised segmentation of histology images via max-min uncertainty. *TMI*, pages 702–714, 2021.
- Yi Li, Yiduo Yu, Yiwen Zou, Tianqi Xiang, and Xiaomeng Li. Online easy example mining for weakly-supervised gland segmentation from histology images. In *MICCAI*, pages 578–587, 2022a.
- Shaoteng Zhang, Jianpeng Zhang, and Yong Xia. Transws: Transformer-based weakly supervised histology image segmentation. In *International Workshop on MLMI*, pages 367–376, 2022.
- Xiaoming Liu, Qi Liu, Ying Zhang, Man Wang, and Jinshan Tang. Tssk-net: Weakly supervised biomarker localization and segmentation with image-level annotation in retinal oct images. *Computers in Biology and Medicine*, page 106467, 2023.
- Ruiwen Xing, Sijie Niu, Xizhan Gao, Tingting Liu, Wen Fan, and Yuehui Chen. Weakly supervised serous retinal detachment segmentation in sd-oct images by two-stage learning. *Biomedical Optics Express*, pages 2312–2327, 2021.
- Tieqiao Wang, Sijie Niu, Jiwen Dong, and Yuehui Chen. Weakly supervised retinal detachment segmentation using deep feature propagation learning in sd-oct images. In *Ophthalmic Medical Image Analysis: 7th International Workshop, OMI 2020*, pages 146–154, 2020c.
- Zhang Chen, Zhiqiang Tian, Jihua Zhu, Ce Li, and Shaoyi Du. C-cam: Causal cam for weakly supervised semantic segmentation on medical image. In *CVPR*, pages 11676–11685, 2022b.
- Jiaqi Yang, Nitish Mehta, Gozde Demirci, Xiaoling Hu, Meera S Ramakrishnan, Mina Naguib, Chao Chen, and Chia-Ling Tsai. Anomaly-guided weakly supervised lesion segmentation on retinal oct images. *Medical Image Analysis*, page 103139, 2024.
- Alec Radford, Jong Wook Kim, Chris Hallacy, Aditya Ramesh, Gabriel Goh, Sandhini Agarwal, Girish Sastry, Amanda Askell, Pamela Mishkin, Jack Clark, et al. Learning transferable visual models from natural language supervision. In *International conference on machine learning*, pages 8748–8763. PMLR, 2021.
- Obioma Pelka, Sven Koitka, Johannes Rückert, Felix Nensa, and Christoph M Friedrich. Radiology objects in context (roco): a multimodal image dataset. In *Intravascular Imaging and Computer Assisted Stenting and Large-Scale Annotation of Biomedical Data and Expert Label Synthesis: 7th Joint International Workshop, CVII-STENT 2018 and Third International Workshop, LABELS 2018, Held in Conjunction with MICCAI 2018, Granada, Spain, September 16, 2018, Proceedings 3*, pages 180–189. Springer, 2018.
- Junnan Li, Dongxu Li, Caoming Xiong, and Steven Hoi. Blip: Bootstrapping language-image pre-training for unified vision-language understanding and generation. In *International conference on machine learning*, pages 12888–12900. PMLR, 2022b.
- Jinheng Xie, Xianxu Hou, Kai Ye, and Linlin Shen. Clims: Cross language image matching for weakly supervised semantic segmentation. In *Proceedings of the IEEE/CVF conference on computer vision and pattern recognition*, pages 4483–4492, 2022b.
- Shaoteng Zhang, Jianpeng Zhang, Yutong Xie, and Yong Xia. Tpro: Text-prompting-based weakly supervised histopathology tissue segmentation. In *International Conference on Medical Image Computing and Computer-Assisted Intervention*, pages 109–118. Springer, 2023.
- Kang Zhou, Yuting Xiao, Jianlong Yang, Jun Cheng, Wen Liu, Weixin Luo, Zaiwang Gu, Jiang Liu, and Shenghua Gao. Encoding structure-texture relation with p-net for anomaly detection in retinal images. In *ECCV*, pages 360–377, 2020.
- Jiaxuan Li, Peiyao Jin, Jianfeng Zhu, Haidong Zou, Xun Xu, Min Tang, Minwen Zhou, Yu Gan, Jiangnan He, Yuye Ling, and Yikai Su. Multi-scale gen-assisted two-stage network for joint segmentation of retinal layers and discs in peripapillary oct images. *Biomed. Opt. Express*, 12(4):2204–2220, 2021. doi: 10.1364/BOE.417212. URL <http://www.osapublishing.org/boe/abstract.cfm?URI=boe-12-4-2204>.
- Jiwoon Ahn, Sunghyun Cho, and Suha Kwak. Weakly supervised learning of instance segmentation with inter-pixel relations. In *CVPR*, pages 2209–2218, 2019.

- 
- Xiao Ma, Zexuan Ji, Sijie Niu, Theodore Leng, Daniel L Rubin, and Qiang Chen. Ms-cam: Multi-scale class activation maps for weakly-supervised segmentation of geographic atrophy lesions in sd-oct images. *IEEE Journal of Biomedical and Health Informatics*, pages 3443–3455, 2020.
- Liang-Chieh Chen, Yukun Zhu, George Papandreou, Florian Schroff, and Hartwig Adam. Encoder-decoder with atrous separable convolution for semantic image segmentation. In *ECCV*, pages 801–818, 2018.
- Jia Deng, Wei Dong, Richard Socher, Li-Jia Li, Kai Li, and Li Fei-Fei. Imagenet: A large-scale hierarchical image database. In *CVPR*, pages 248–255, 2009.
- N Reimers. Sentence-bert: Sentence embeddings using siamese bert-networks. *arXiv preprint arXiv:1908.10084*, 2019.